AGU PUBLICATIONS

JGR

Journal of Geophysical Research: Solid Earth

RESEARCH ARTICLE
10.1002/2017JB014964

Key Points:
- The damage precursory to failure in a quartz-monzonite rock is imaged at micrometer resolution
- A power law increase of damage rate and largest microfracture characterizes the road to faulting; failure stress is a critical point
- Variations in the shape parameters of microfractures are quantified and provide a new characterization of precursors to failure

Supporting Information:
- Supporting Information S1
- Movie S1
- Movie S2

Correspondence to:
F. Renard,
francois.renard@geo.uio.no

Citation:
Renard, F., Weiss, J., Mathiesen, J., Ben-Zion, Y., Kandula, N., & Cordonnier, B. (2018). Critical evolution of damage toward system-size failure in crystalline rock. *Journal of Geophysical Research: Solid Earth*, *123*, 1969–1986. https://doi.org/10.1002/2017JB014964

Received 9 SEP 2017
Accepted 3 FEB 2018
Accepted article online 8 FEB 2018
Published online 21 FEB 2018

Critical Evolution of Damage Toward System-Size Failure in Crystalline Rock

François Renard[1,2], Jérôme Weiss[2], Joachim Mathiesen[3], Yehuda Ben-Zion[4], Neelima Kandula[1], and Benoît Cordonnier[1,5]

[1]The NJORD Center, Department of Geosciences, University of Oslo, Oslo, Norway, [2]Université Grenoble Alpes, Université Savoie Mont Blanc, CNRS, IRD, IFSTTAR, ISTerre, Grenoble, France, [3]Niels Bohr Institute, University of Copenhagen, Copenhagen, Denmark, [4]Department of Earth Sciences, University of Southern California, Los Angeles, CA, USA, [5]ESRF—The European Synchrotron, Grenoble, France

Abstract Rock failure under shear loading conditions controls earthquake and faulting phenomena. We study the dynamics of microscale damage precursory to shear faulting in a quartz-monzonite rock representative of crystalline rocks of the continental crust. Using a triaxial rig that is transparent to X-rays, we image the mechanical evolution of centimeter-size core samples by in situ synchrotron microtomography with a resolution of 6.5 μm. Time-lapse three-dimensional images of the samples inside the rig provide a unique data set of microstructural evolution toward faulting. Above a yield point there is a gradual weakening during which microfractures nucleate and grow until this damage span the whole sample. This leads to shear faults oriented about 30° to the main compressive stress in agreement with Anderson's theory and macroscopic failure. The microfractures can be extracted from the three-dimensional images, and their dynamics and morphology (i.e., number, volume, orientation, shape, and largest cluster) are quantified as a function of increasing stress toward failure. The experimental data show for the first time that the total volume of microfractures, the rate of damage growth, and the size of the largest microfracture all increase and diverge when approaching faulting. The average flatness of the microfractures (i.e., the ratio between the second and third eigenvalues of their covariance matrix) shows a significant decrease near failure. The precursors to faulting developing in the future faulting zone are controlled by the evolving microfracture population. Their divergent dynamics toward failure is reminiscent of a dynamical critical transition.

1. Introduction

Detailed processes of rock failure and the possible existence of precursory activity depend on mechanisms and heterogeneities that span a wide range of spatial scales, from microns associated with individual grains to hundreds of kilometers associated with large continental faults (see, e.g., Figure 1 in Ben-Zion, 2008). At the field scale, several examples of precursors to earthquakes or rock falls have been reported by monitoring seismic activity (Amitrano et al., 2005; Bouchon et al., 2011, 2013; Jones & Molnar, 1979; Kato et al., 2016; Sugan et al., 2014), although precursory events have not been detected in other cases (Wu et al., 2014). Rupture instabilities of large earthquakes occur in most cases along preexisting faults. Macroscopic faulting corresponds to the formation of a slip surface or zone by the linkage of smaller defects to the tip of a growing fault (Candela & Renard, 2012; Cowie & Scholz, 1992; Otsuki & Dilov, 2005). In the laboratory, acoustic emission can be used to monitor the development of faults at the decimeter scale in quartz-rich rocks (Goebel et al., 2012; Lockner et al., 1991; Schubnel et al., 2007; Zang et al., 2000). This technique also gives information on the evolution of the velocities, dispersion, and anisotropy of elastic wave propagation (Hamiel et al., 2009; Schubnel & Guéguen, 2013). However, acoustic emission studies have the following limitations: (i) a limited spatial resolution usually of several millimeters, (ii) no detection of quasi-static damage growth, (iii) limited information on microscopic geometry of individual damage events, and (iv) the necessity to calibrate the acoustic sensors and use a model to invert for the size and source parameters of the microfractures. To overcome these limitations, another imaging technique, with X-ray adsorption and phase contrast microtomography, has been developed in the past 20 years and is now becoming routinely used in rock physics experiments to image samples either after deformation (e. g. Benson et al., 2008; Desrues et al., 1996; Renard et al., 2009) or more recently in situ and time-lapse during deformation (Renard et al., 2004, 2017; Zhu et al., 2016). This technique has the advantages of high spatial resolution, down to submicron scales, and allows measuring directly the total strain and local damage inside the sample (i.e., seismic plus aseismic). Here we use a triaxial rig that is

Table 1
Experimental Conditions With Temperature (T), Confining Pressure (P_c), Pore Fluid Pressure (P_p), Yield Stress, Differential Stress at Failure (σ_f), and Number of Three-Dimensional X-ray Tomography Volume Scans Acquired During Each Experiment

Sample	*T*	P_c	P_p	Yield stress	σ_f	Nb. scans
Monzonite 3	25°C	20 MPa	0 MPa	219 MPa	253 MPa	62
Monzonite 4	25°C	35 MPa	5 MPa	249 MPa	276 MPa	64

transparent to X-rays and that allows imaging at high spatio-temporal resolution a rock core sample under in situ stress conditions corresponding to several kilometer depths and in the presence of water. This allows identifying all microfractures with size larger than the 6.5 μm resolution of the imaging technique, and statistical characterization of the damage evolution toward failure. For the first time, such dynamic three-dimensional experiments provide data (i) to characterize the dynamics of precursors to faulting in a rock representative of the continental crust, (ii) to image fault initiation and growth, (iii) to test physical models of fracturing and faulting (see reviews by Ben-Zion, 2008, and de Arcangelis et al., 2016), and specifically whether rock rupture dynamics is controlled by the existence of a critical point close to failure (e.g., Alava et al., 2006; Fisher et al., 1997; Girard et al., 2010; Jaumé & Sykes, 1999; Rundle et al., 2003; Sornette & Sammis, 1995, and references therein).

Following the definition used for various physical systems, a critical behavior refers to the dynamics of observables that change abruptly when a parameter, called a control parameter, approaches a critical value (called critical point). In the present study the control parameter is the stress in the solid. Critical systems are characterized by the emergence of scaling relationships among several quantities and power law distribution functions of various quantities (Christensen & Moloney, 2005).

2. Materials and Methods

Two core samples of a quartz-monzonite block with dimensions of 4 mm diameter and 10 mm height are analyzed. This crystalline rock contains 17.9% quartz, 12.8% biotite, 57.6% plagioclase (38% anorthite), 11.7% clinopyroxene, and small amounts of minor minerals. The mean grain size is 450 μm, and the initial porosity is low, close to 0.8% (Aben et al., 2016). The parameters of this rock are Young's modulus of 25.6 ± 0.3 GPa, Poisson's ratio of 0.25, and initial porosity of 0.78 ± 0.3%. The composition and mechanical properties of this rock are representative of other continental crystalline rocks such as granites. The two samples are deformed in a triaxial apparatus that is transparent to X-rays, called "HADES" (Renard et al., 2016, 2017), installed on the microtomography beamline ID19 at the European Synchrotron Radiation Facility. This experimental technique allows imaging with X-rays the sample directly inside the rig during its deformation toward failure at different time steps, providing time-lapse results. The voxel size is 6.5 μm, which is close to the spatial resolution of the imaging technique. When using the full white beam of the synchrotron with energy close to 200 keV, the average beam energy that crosses the sample is close to 120 keV because the triaxial rig adsorbs a significant proportion of the X-rays. The experiments are performed at room temperature under constant confining pressure and constant pore fluid pressure (Table 1). In the HADES rig (a sketch of the apparatus is provided in Renard et al., 2016), the sample is surrounded by a jacket made of Viton polymer on which the confining pressure is applied by pressurized oil. The sample is installed between two stainless steel pistons: the lower piston is immobile and the axial load is imposed on the upper piston that can move vertically. The axial load and confining pressure are controlled independently by two pumps. A central hole in the two pistons allows injecting water as a pore fluid. The pore fluid pressure is controlled by two pumps connected one at the inlet and the other one at the outlet, at each extremity of the sample. During each experiment, the axial stress is increased step by step. After each step when the sample is at rest and the stress reaches a constant level, a three-dimensional image is acquired. The experiment is stopped when the sample fails and a final image is then acquired after stress release. Each X-ray tomography acquisition lasts for 1.5 min. More than 60 three-dimensional volumes are acquired for each sample, at 32 bytes grayscale resolution of X-ray adsorption. From the X-ray radiographs, three-dimensional volumes are reconstructed using both X-ray adsorption and phase contrast (Mirone et al., 2014). During the reconstruction, corrections are applied to remove acquisition noise, including ring artifacts, and to correct for variations of intensity of the X-ray source during the experiment. The final data set is a time series of three-dimensional volumes for each experiment, from which axial strain and damage prior to failure can be extracted (Figures 1 and S1 and Movies M1 and M2).

These data are analyzed using the commercial image analysis software AvizoFire™, and the following procedure is applied. First, all three-dimensional volumes are denoised using a nonlocal-means filter (Buades et al., 2005). Second, a mask is applied to remove the jacket and confining oil around the sample. Third, because of

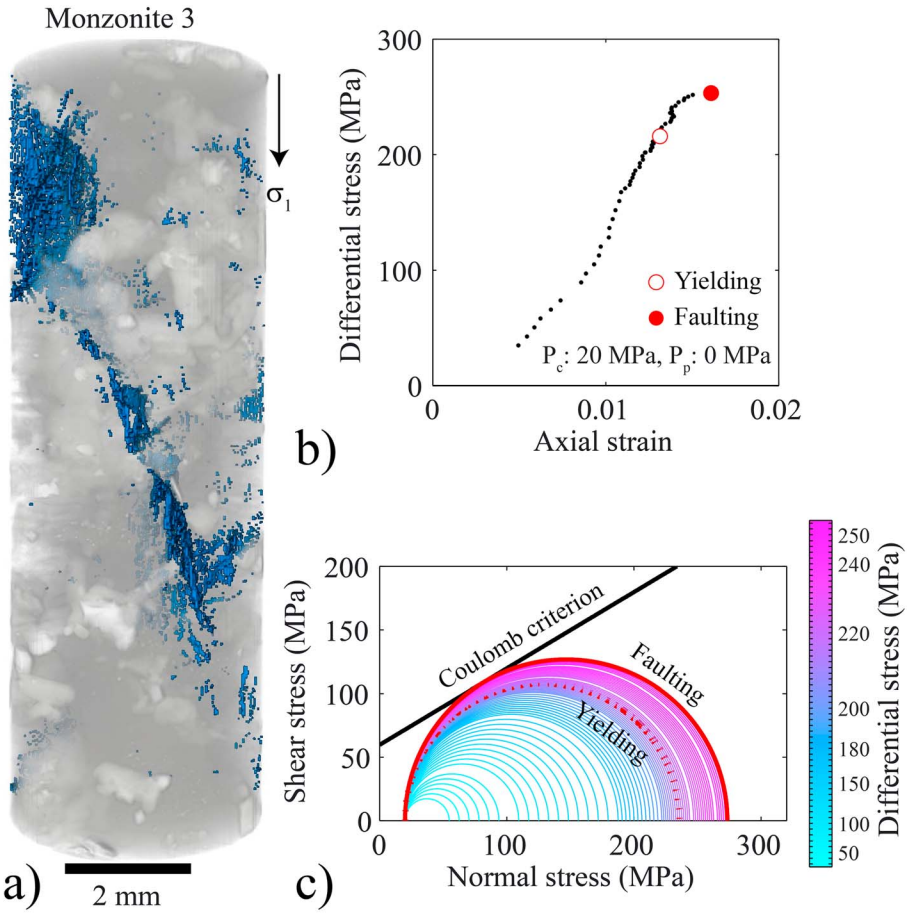

Figure 1. Experimental data for sample Monzonite 3. (a) Three-dimensional rendering of the sample at the onset of faulting. The rock is rendered partly transparent, and the damage is shown in blue. (b) Differential stress-strain curve with each dark dot corresponding to one stress step and one three-dimensional X-ray microtomography acquisition. Onset of yielding and onset of faulting are shown. P_C: confining pressure. P_P: pore pressure. (c) Mohr diagram with each circle corresponding to one stress step shown in (b). The Coulomb failure criterion, the onset of yielding, and the onset of faulting are displayed. A time-lapse animation of the development of the damage is shown in Movie M1.

the high resolution of X-ray adsorption, the voxels that contain air (i.e., voids) can be isolated from the rest of the rock by a simple thresholding procedure. The same grayscale threshold is applied for the whole series of three-dimensional images on each sample to extract all the voids (cavities, pores, and microfractures) in the sample during deformation. Here we call a void an ensemble of voxels that are connected and forms a single object filled with air or water. Each of these voids, which we call damage, is labeled and its geometrical characteristics are calculated (position, volume, surface area, covariance matrix, orientation, and shape parameters). This analysis of individual damage is performed using the built-in function "label analysis" of the software AvizoFire™. As a result a list of individual damage at each stress step is obtained and their statistics can be analyzed in details. Due to the limited spatial resolution of 6.5 μm, microcracks with an opening smaller than half of the resolution (3.2 μm) cannot be extracted. For example, as shown in Figure 2, the main cracks could be separated from their grayscale level. However, thinner cracks, even if visible on the grayscale image, have insufficient contrast to be separated from the surrounding grain. As a consequence, the results of the present study involve only damage whose aperture is above the detection limit of 3.2 μm. When two microfractures coalesce, which happen very near failure, they are considered as a single fracture in the analyses. However, in addition to coalescence events, the number of microfractures grows until failure (Figure S2) and therefore nucleation of new microfractures continues to occur until failure.

The geometrical properties of each microfracture can also be estimated. Some of these measurements are represented in Figure 2c. For each microfracture, the three-dimensional covariance matrix is calculated to

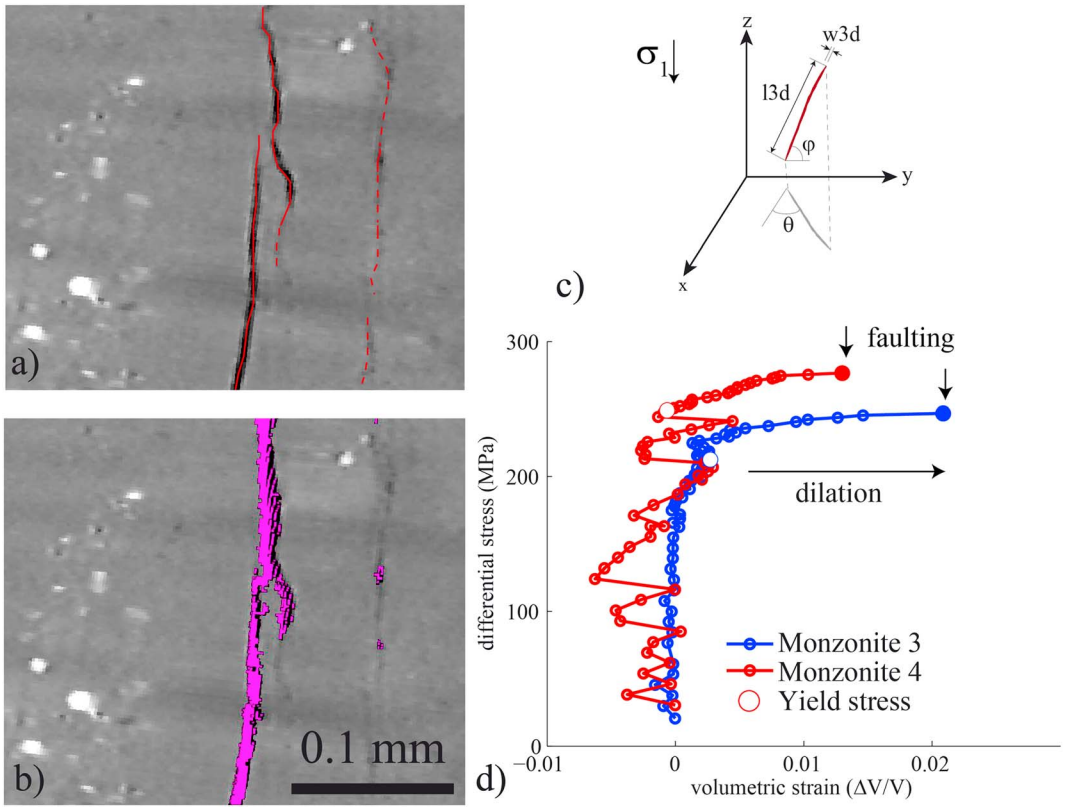

Figure 2. Zoom on several microcracks at the onset of failure in the sample Monzonite 3. (a) Two-dimensional vertical slice parallel to σ_1 shows microcracks with various apertures. The dashed red lines underline cracks whose aperture is so small that they cannot be segmented. (b) Three-dimensional view of the microfractures after segmentation. (c) Three-dimensional geometric parameters measured on a microfracture represented in purple: length along the largest axis (l3d, measured by the largest eigenvalue δ_1), width perpendicular to the largest axis (w3d, measured by the smallest eigenvalue δ_3), and orientation with the angles θ and φ calculated by projecting the microfracture on the *x-y* plane (fracture projection represented in gray). The main compressive stress σ_1 is parallel to the *z* axis. (d) Volumetric strain for the two samples measured by calculating the evolution of the volume using the 3D images. A dilatant behavior is observed when approaching failure.

determine the three eigenvalues of the object $\delta_1 > \delta_2 > \delta_3$ and its orientation. The eigenvalues quantify the extent of the object along its three principal directions. If the object was a perfect ellipsoid, δ_1 would represent the extent of the longest axis, δ_2 of the intermediate one, and $\delta_3$of the shortest one. The longest dimension of a microfracture is given by δ_1 (Figure 2c). The angles φ and θ measure the orientation of the largest eigenvector of a given microfracture in spherical coordinates (Figure 2c). If $\varphi = 90^{\circ}$, the microfracture is parallel to σ_1; if $\varphi = 0^{\circ}$, it is perpendicular to σ_1. The angle θ varies in the range (−180°–180°) and measures the orientation of the projection of the object in a plane perpendicular to σ_1. From these parameters, several additional geometrical parameters for each microfracture can be calculated. The anisotropy, defined as $1 - \delta_3/\delta_1$, measures the deviation from a spherical shape and is equal to 0 for a sphere and tends to 1 for planar objects. The elongation is defined as δ_2/δ_1 and tends to 0 for elongated objects. The flatness is defined as δ_3/δ_2 and tends to 0 for flat objects. Finally, the three-dimensional shape factor is defined as VA3d $= \frac{S^3}{36\pi V^2}$, where *S* is the surface area of the three-dimensional object and *V* is its volume; VA3d is equal to 1 for a sphere. At the macroscopic scale, the development of damage induces a dilation of the whole rock sample when approaching faulting (Figure 2d).

3. Results

Four kinds of results are discussed in this section. First, the strain-stress evolution of the samples toward faulting is presented (Figures 1 and S1 and Movies M1 and M2). Second, rock damage and the evolution of

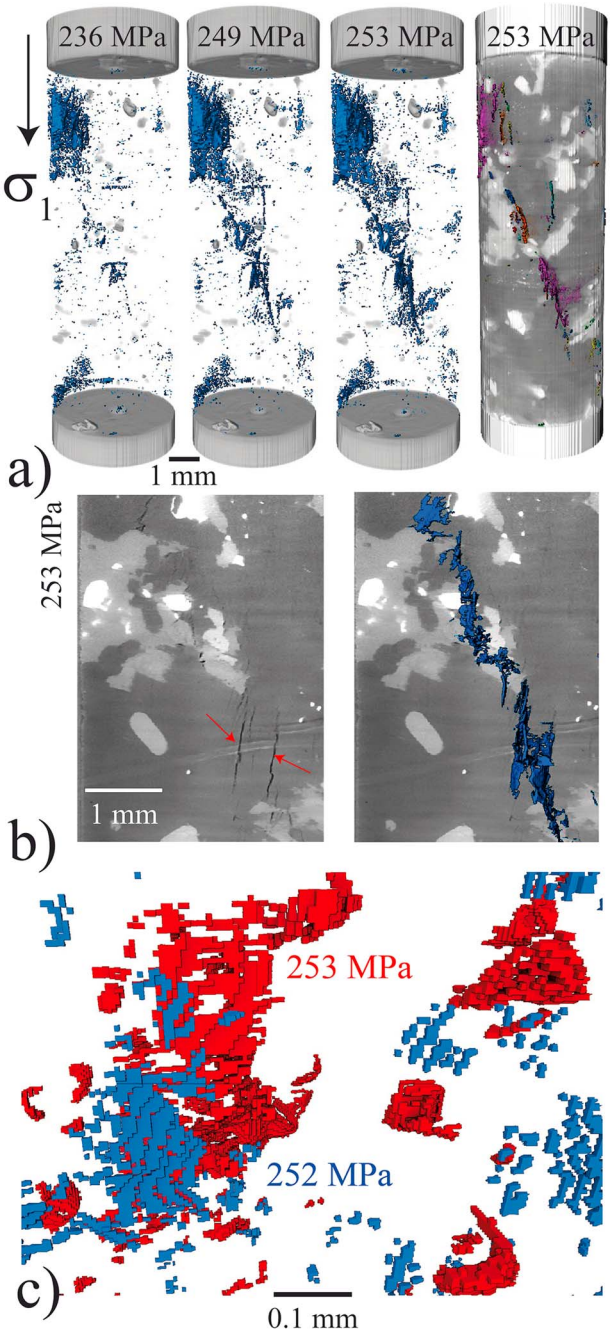

Figure 3. Development of damage in the sample Monzonite 3. The main compressive stress σ_1 is vertical on all images. (a) Three-dimensional rendering of the evolution of damage with increasing differential stress from 236 to 253 MPa. For the first three images, the rock is made transparent and the damage is colored in blue. For the last image in the row, each individual microfracture is labeled with a different color and the rock is displayed partly transparent in gray. (b) Zoom on the damage at the onset of faulting with microfractures indicated as red arrows on the left and three-dimensional rendering of the microfractures that align along the future shear fault plane on the right. (c) Zoom (3D rendering) inside the sample showing several microfractures at 252 MPa (blue) and the difference between 253 and 252 MPa (in red), 253 MPa being the differential stress at the onset of failure. Damage volume increases by two processes: nucleation of new microfractures and growth of existing microfractures.

microfractures toward faulting are described qualitatively (Figures 3 and 4 and Movies M1 and M2). In a third subsection, the global properties of damage, damage rate, and largest microfracture are quantified (Figures 5, 6, and S2). Finally, the statistics of damage geometry are analyzed in detail in the last section (Figures 7 and 8). If the results of the first two sections reproduce existing knowledge about rock faulting, the data of the last two sections are unique because, for the first time, they allow a detailed quantification of the precursors to faulting due to the high spatial resolution of the time-resolved X-ray microtomography imaging technique.

3.1. Stress-Strain Evolution

The two samples failed by shear faulting with stress-strain curves following the typical mechanical behavior of crystalline rocks (Figures 1 and S1 and Movies M1 and M2). The axial strain is measured directly on the three-dimensional images from the height of the sample. The differential stress σ is calculated as $\sigma = \sigma_1 - P_c + P_p$, where σ_1 is the axial load, corresponding to the main compressive stress; P_c is the confining pressure; and P_p is the pore fluid pressure. At low differential stress, the relationship between differential stress and strain is nonlinear, which can be explained by the closing of preexisting microfractures in the sample. This effect is clearly visible in the sample Monzonite 4 where a horizontal microfracture closes during the first steps of stress increase (Movie M2). With increasing axial load, the stress-strain relationship shows a linear trend, corresponding to the elastic deformation of the rock. At the yield point (219 MPa for sample Monzonite 3 and 249 MPa for sample Monzonite 4), the stress-strain curve starts to deviate from linearity and the apparent elastic modulus decreases progressively until the failure point is reached (Figures 1 and S1). These stress-strain relationships are similar to those of other rocks (Paterson & Wong, 2005). The Mohr circles corresponding to the successive stress steps are also represented (Figures 1c and S1c). In these two figures, the Coulomb failure criterion is represented as a straight line associated with internal friction angle of 0.6 (not measured) and cohesion close to 60 MPa. However, the concept of Coulomb failure criterion does not account for the observed precursory damage before failure. The onset of yielding, represented as a red dashed line on Figures 1c and S1c, underlines the domain where damage develops prior to failure.

3.2. Pattern of Damage

The evolution of damage when approaching faulting is shown in Figure 3. At the onset of yielding, microfractures start nucleating and growing in the volume, and some will eventually participate to the future fault zone (Figure 3a). At the onset of failure, corresponding to a differential stress of 253 MPa for sample Monzonite 3 (Table 1), the microfractures are mostly oriented parallel to σ_1 (Figure 3b), and their linkage will later induce the failure of the sample. Most of these microfractures are transgranular, and several can be pinned at grain boundaries. Because it is possible to follow the evolution of damage and differentiate successive three-dimensional images, the increments of damage can be followed at the onset of yielding and failure for the sample Monzonite 3. The damage is observed to expand by two processes: the nucleation of new microfractures and the extension of

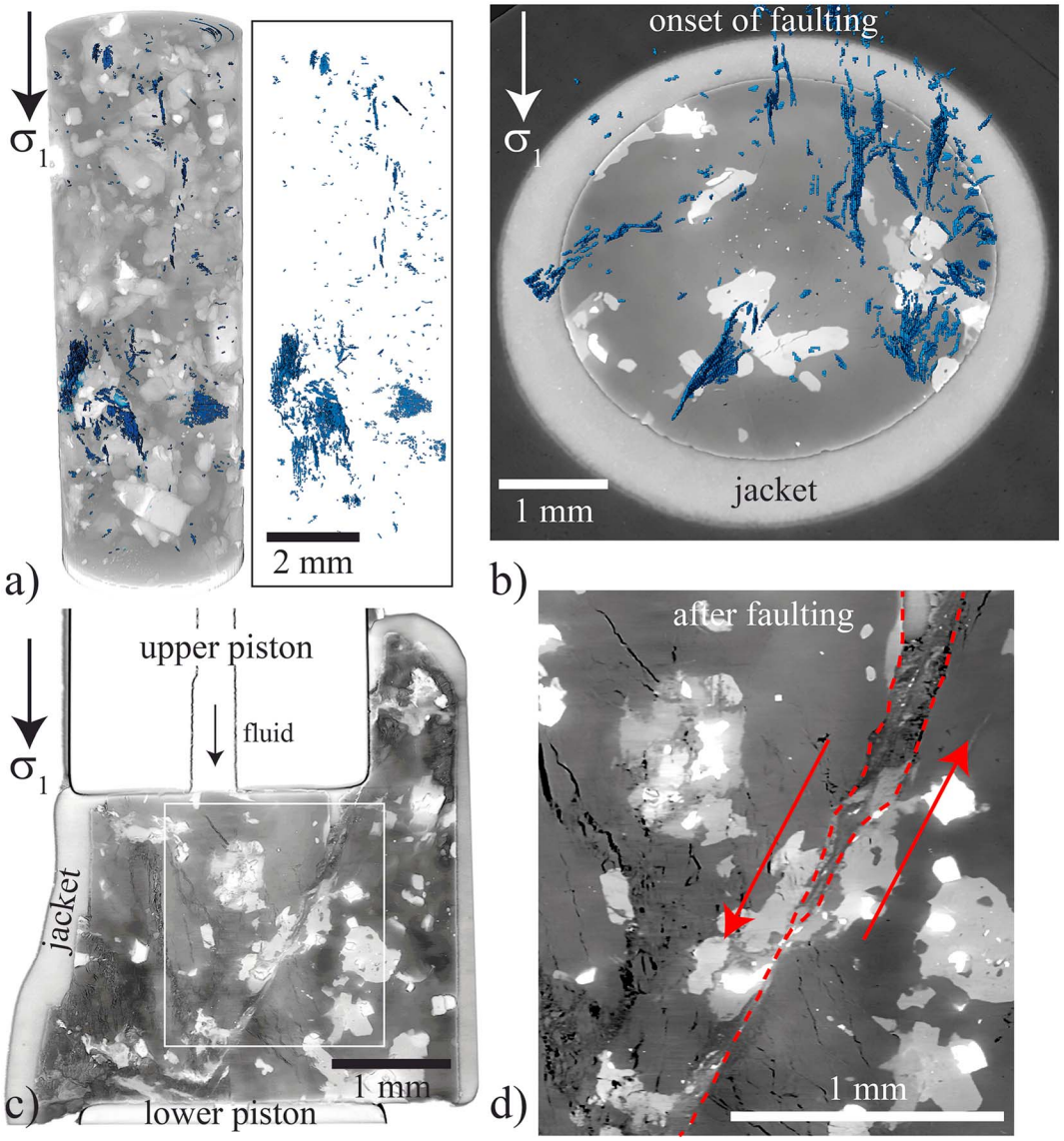

Figure 4. (a and b) Damage at the onset of faulting and (c and d) sample after faulting for sample Monzonite 4. (a) Views of the damage (blue) at the onset of faulting with two different three-dimensional rendering: the rock sample in partly transparent gray with the damage represented in blue (left) and the damage only (right). (b) Two-dimensional horizontal slice and three-dimensional damage at the onset of faulting showing that most microfractures are oriented parallel to σ_1 and oriented in all angles in a plane perpendicular to σ_1. The Viton jacket surrounding the sample is shown. (c) Two-dimensional vertical slice in the center of the sample after shear faulting which occurred abruptly after increasing the axial stress by 1 MPa after the views displayed in (a) and (b). The axial, confining, and pore pressures were released to open the cracks. The moving upper piston and immobile lower piston, with the internal channels for pore fluid injection, are shown. (d) Zoom on the shear fault underlined with a dashed red line. The field of view corresponds to the white rectangle shown in (c).

existing microfractures (Figure 3c). For sample Monzonite 4, with controlled pore fluid pressure of 5 MPa, the growth of damage follows the same pattern (Figure 4a). Above the yield point microfractures nucleate, grow, and cluster in two zones that evolve later into conjugate faults. These mode I microfractures are oriented mostly in the vertical direction, parallel to σ_1, and cover a wide range of orientations in a plane perpendicular to σ_1 and parallel to the confining stress direction (Figure 4b). They form en echelon arrays until coalescence (Du & Aydin, 1991).

After failure, the loading on the samples is released to open the cracks and a three-dimensional scan is acquired to image the generated shear fault zones (Figure 4c). Both samples fail along a set of

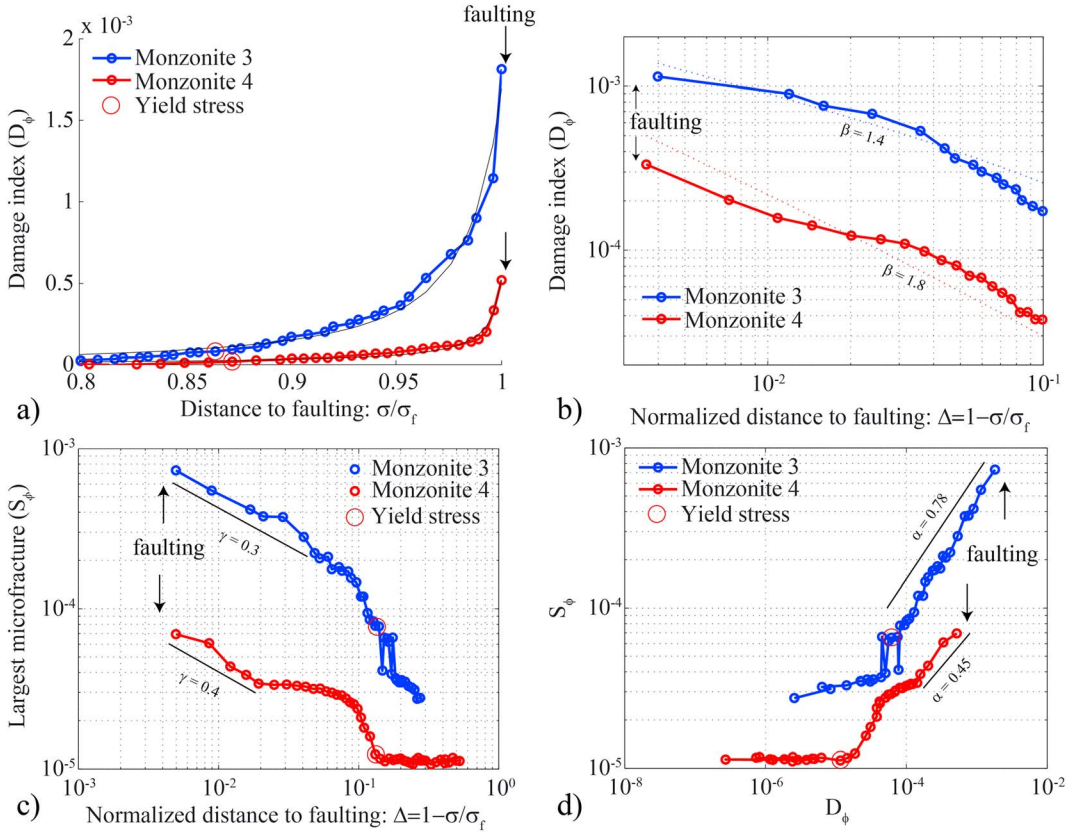

Figure 5. The road to failure. (a) Evolution of the total volume of damage (i.e., microfractures) as a function of the distance to failure. The damage index D_ϕ is dimensionless and represents the porosity (i.e., void ratio) of the sample ϕ compared to the initial porosity. The dark lines show the best fits according to the equation below. (b) Same data as in (a) where the horizontal axis is the normalized distance to failure $\Delta = \left(\frac{\sigma_f - \sigma}{\sigma_f}\right)$. The dashed lines correspond to $D_\phi \sim \frac{1}{(\beta-1)}\left[\Delta^{-(\beta-1)} - 1\right]$, with $\beta = 1.4$ for sample Monzonite 3 and 1.8 for sample Monzonite 4. (c) Evolution of the size of the largest microfracture S_ϕ toward failure. (d) S_ϕ as a function of D_ϕ in a log-log plot. On these plots, the yield point shown in the differential stress-strain curve (Figures 1 and S1) is represented as an open red circle.

well-localized conjugate shear faults. For sample Monzonite 4, one of the fault shows some branching with two slip surfaces (dashed lines in Figure 4c) that separate a region with grain comminution. These two faults delimitate a lens of deformed material, reminiscent of lenses observed at outcropping faults (Candela & Renard, 2012; Lindanger et al., 2007). Outside this region, the thickness of the fault zone is quite small and within one or two voxels, that is, less than 10 μm thick, showing extreme localization. A large number of microcracks oriented parallel or conjugate to the main fault surface have formed (Figure 4c, right).

3.3. Global Evolution of Damage Toward Failure

The approach to failure is measured by the evolution of three quantities when approaching σ_f: the total volume of the damage measured by a damage index, the rate of increase of this damage, and the size of the largest microfracture (Figure 5). The dimensionless damage index is defined as $D_\phi = \frac{\phi - \phi_i}{1 - \phi_i}$, where ϕ_i is the initial porosity (i.e., void fraction) of the sample before loading is applied and ϕ is the porosity at a given stress step, this porosity resulting from the nucleation and growth of microfractures. The size of the largest microfracture, L_ϕ, also called largest cluster in reference to percolation theory (see section 4.1), is defined as its volume divided by the entire volume of the sample and is also dimensionless. From the experiments, one can only obtain a lower estimate, $\widehat{\sigma}_f = \sigma_f - \epsilon$ of the stress at faulting σ_f, which is the last stress measured during the tomography scan before macroscopic failure occurs. Therefore, in the estimate of the failure stress, an offset ε of the order of $0.005\sigma_f$ is introduced. When σ_f is approached, an acceleration of damage is

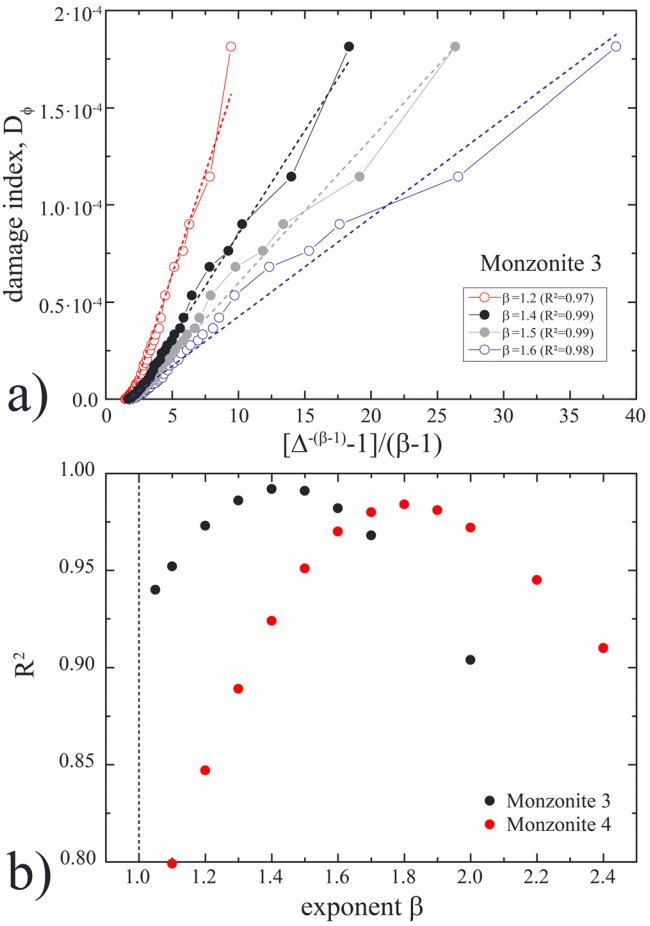

Figure 6. Evaluation of the scaling of the damage growth rate $\frac{dD_\phi}{d\Delta} \sim \Delta^{-\beta}$. (a) Plot of the relationship $D_\phi \sim \frac{1}{(\beta-1)} \left[\Delta^{-(\beta-1)} - 1\right]$ for sample Monzonite 3 and for several values of the exponent β. (b) Variation of the coefficient of determination R^2 of the various fits shown in (a) and corresponding to different values of β. The highest R^2 corresponds to a β-value of 1.4 for Monzonite 3 and 1.8 for Monzonite 4.

observed (Figure 5a). We first conjecture that this acceleration is a consequence of a power law divergence of the damage *rate* with stress (rather than strain) when approaching faulting:

$$\frac{dD_\phi}{d\Delta} \sim -\Delta^{-\beta}, \tag{1}$$

where $\Delta = \left(\frac{\sigma_f - \sigma}{\sigma_f}\right)$ is defined as the normalized distance to faulting, β a critical exponent, and the negative sign on the right-hand side of equation (1) comes from the definition of Δ (decreasing as approaching faulting). The term *divergence* refers here to unbounded growth of a variable in an infinite system or to a finite value in finite-size systems, when approaching a critical value of Δ (Alava et al., 2006). An integration of (1) from the onset of loading ($\Delta = 1$; $D_\phi = 0$) gives

$$D_\phi \sim \frac{1}{(\beta - 1)} \left[\Delta^{-(\beta-1)} - 1\right]. \tag{2}$$

As D_ϕ is observed to accelerate before faulting (Figure 5a), β is necessarily larger than 1. We searched for the β-value maximizing the linear fit between D_ϕ and $[\Delta^{-(\beta\ -\ 1)} - 1]$ and found a value of $\beta = 1.4$ for Monzonite 3 and $\beta = 1.8$ for Monzonite 4 (Figure 6). The goodness of fit ($R^2 > 0.99$ for Monzonite 3, $R^2 > 0.98$ for Monzonite 4) implies that our initial conjecture (1) is a good model for the data throughout the entire tests, from the onset of damage to final faulting. This also implies that near final failure ($\Delta \rightarrow 0$), the damage index diverges as well, $D_\phi \sim \Delta^{-\beta\ +\ 1}$, though with a smaller exponent $\beta - 1 = 0.4$ to 0.8 (Figure 5b). Note that a direct estimation of $\beta - 1$ from an analysis of the power law scaling of D_ϕ near failure would be less reliable, because of the integration constant -1 in the brackets of equation (2).

We then looked at the evolution of the largest microfracture/cluster, S_ϕ, and found, for $\Delta < 0.15$, a scaling $S_\phi \sim D_\phi^{\alpha}$, with $\alpha = 0.78 \pm 0.03$ for Monzonite 3 and $\alpha = 0.45 \pm 0.03$ for Monzonite 4 (Figure 5d). Note that this nontrivial scaling ($\alpha \neq 1$) already rules out single-crack mechanisms of faulting (see below). This also suggests a divergence of S_ϕ toward faulting as well, $S_\phi \sim \Delta^{-(\beta\ -\ 1)\alpha}$, with an exponent $\gamma = (\beta - 1)\alpha$ between 0.3 and 0.4 for both samples. This is well supported by the data (Figure 5b). Note that we also tried to fit an exponential growth toward faulting, and the fits are of lower quality than with a power law divergence, that is, twice higher root-mean-square residuals for the same number of fitting parameters. As discussed in the section 4, a power law evolution of damage and/or of the size of the largest microfracture toward system-size failure is consistent with models where the establishment of long-range correlations in the stress field lead to a critical phenomenon (e.g., de Arcangelis et al., 2016, and references therein). These models have been proposed to explain intermittent critical behavior of large earthquake dynamics (Ben-Zion et al., 2003; Jaumé & Sykes, 1999; Sammis & Smith, 1999).

3.4. Statistics of Damage Geometry Toward Failure

For each three-dimensional image, the microfractures can be extracted and labeled, allowing calculations of their geometrical properties. Two kinds of data can be represented to characterize the evolution toward failure: the mean value of a given geometrical property (Figure 7, Table 2) and the probability density functions of properties in all three-dimensional images at each stress step between the onset of yielding and failure (Figure 8).

The cumulative distribution of damage sizes has been calculated, where the size of a given damage void is defined as its volume (Figures 8a and 8b). These data show that some voids, which correspond to preexisting defects (pores and microfractures) in the sample, are already present at the yield point. For sample Monzonite

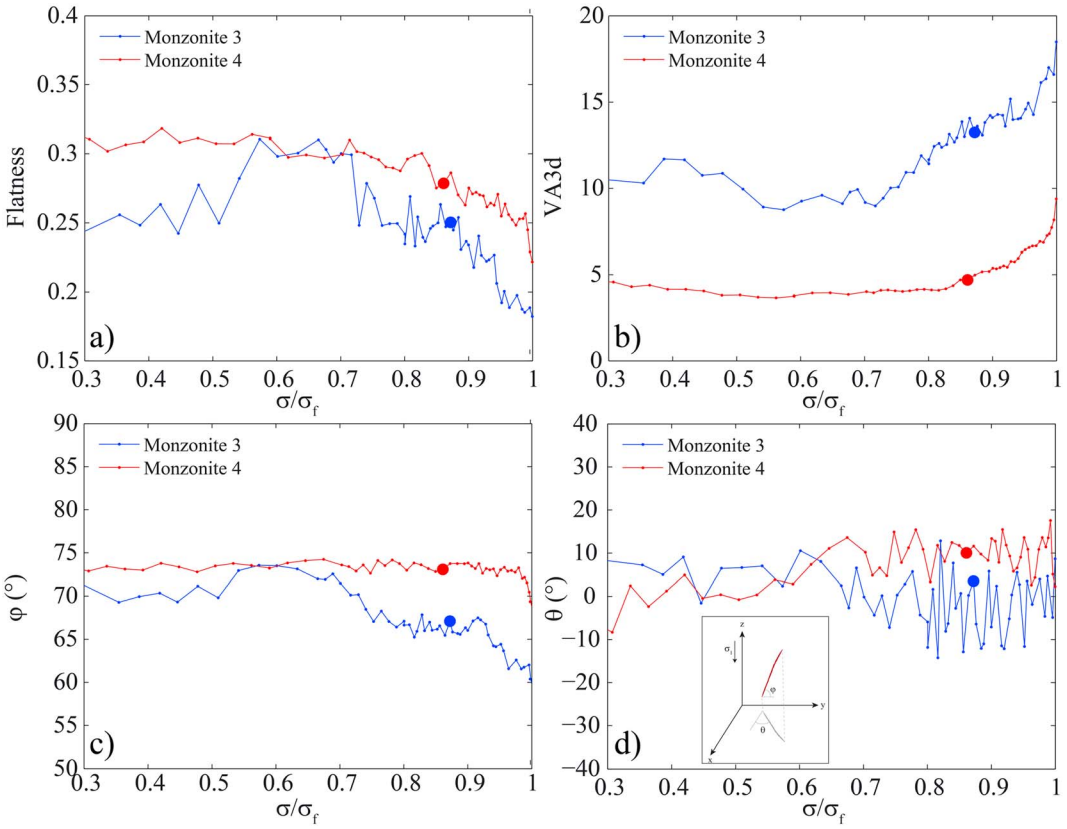

Figure 7. Evolution of four geometrical parameters of microfractures toward stress at faulting σ_f. Each dot corresponds to data of one three-dimensional image. The full circles indicate yield points in the stress-strain curves (Figures 1 and S1). (a) Mean flatness of the microfractures. (b) Three-dimensional shape factor (VA3d). (c) Angle φ of the microfractures. (d) Angle θ of the microfractures. The inset shows the definition of the angles φ and θ. Failure occurred at $\sigma/\sigma_f = 1$. Note the significant decrease of flatness and increase of VA3d when approaching faulting (see Table 2). The angle ϕ decreases due to linkage of mostly vertical microcracks, whereas the average value of the angle θ does not change toward faulting. The probability density functions of the flatness, angle φ, and angle θ are displayed on Figure 8.

3, the slope of the cumulative void volume distribution in a log-log scale does not evolve significantly (Figure 8a). Conversely, for sample Monzonite 4, there is a clear evolution with increasing slope when approaching failure (Figure 8b). For both samples, larger voids are formed between the yield point and failure, corresponding to the growth of the largest microfractures identified in Figures 4 and 5.

The average values of the three eigenvalues of the covariance matrix $\delta_1 > \delta_2 > \delta_3$ show a significant increase toward failure (Table 2 and Figure S3). This confirms the growth of damage in the sample. The anisotropy and the elongation of the microfractures do not show significant variations toward failure (Table 2). The anisotropy, which measures the deviation from a sphere, remains constant, indicating that most of the damage occurs through approximately planar defects throughout the entire faulting process. The elongation, which measures the ratio between the longest axis and the intermediate axis of an object, remains constant. This indicates that the microfractures keep the same proportions in these two directions, although they are longer in the direction parallel to σ_1. The third geometrical parameter, the flatness δ_3/δ_2, shows a clear evolution toward failure and decreases by more than 20% for both samples (Table 2 and Figure 7a). From the evolution of these three parameters, it can be concluded that the damage develops on average as planar microcracks, with extension parallel to σ_1 larger than in the two other perpendicular directions. An expanding fracture can either dilate (opening perpendicular to the local σ_3, without generation of new surface area) or increase dimensions along σ_1, or increase size along σ_2, both with increasing surface area. Interestingly, when approaching failure, the flatness shows a significant decrease indicating that the microfractures deform by expanding more along the local intermediate principle direction σ_2 than by increasing aperture. In other words, because the flatness is decreasing, microfractures grew more along local σ_1 and σ_2 directions than

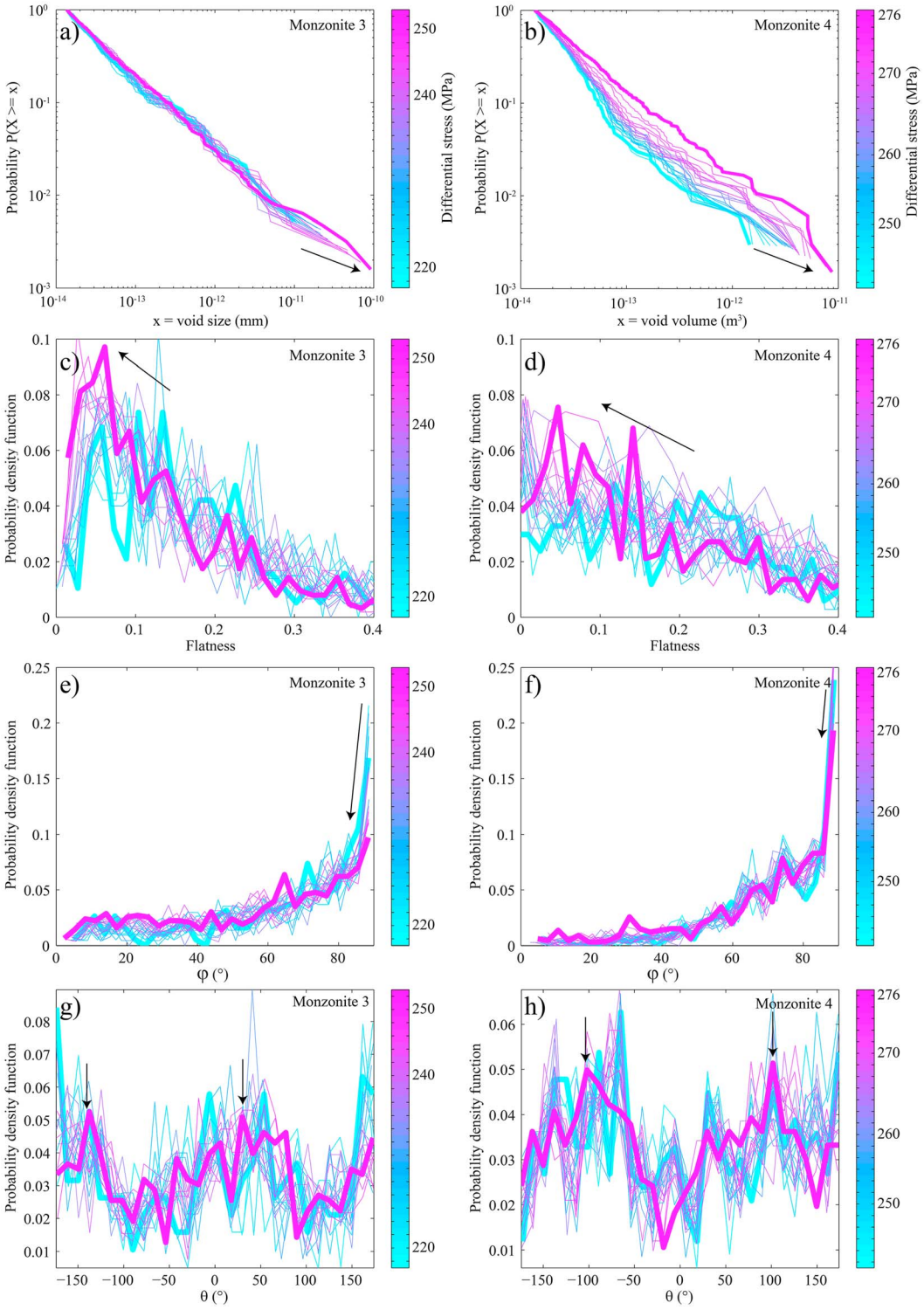

Figure 8. Evolution of distributions of the geometrical properties of damage between the yield point and failure. On each plot, the thick curves correspond to the distribution at yield stress (blue) and the distribution at the stress of faulting (purple), respectively. The black arrows indicate the evolution toward failure. Average values are displayed in Figure 7. (a and b) Cumulated distribution of void volume for samples Monzonite 3 and Monzonite 4, respectively. Here the void volume corresponds as the volume of each microfracture and pore. When approaching failure, the sizes of the largest microfractures increase (black arrows). (c and d) Probability density function of the flatness parameter. The arrows point to the decrease of microfracture flatness when approaching faulting. (e and f) Probability density function of the angle φ defined in Figure 2c. The arrows point to the decrease of the average angle when approaching failure and interpreted at the linkage of mostly vertical microfractures. (g and h) Probability density distribution of the angle θ defined in Figure 2c. The arrows point to directions corresponding to the development of macroscopic shear faults.

Table 2
Variation of the Mean Value of Relevant Geometrical Parameters of the Microfractures Between Yield Stress and Failure

Parameter	Monz. 3, yield	Monz. 3, σ_f	Variation	Monz. 4, yield	Monz. 4, σ_f	Variation
δ_1 (voxel)	84	115	**+37%**	88	145	**+65%**
δ_2 (voxel)	16	24	**+50%**	6	17	**+183%**
δ_3 (voxel)	1.6	3.9	**+144%**	0.94	1.4	**+49%**
Flatness	0.25	0.18	**−28%**	0.28	0.22	**−21%**
Anisotropy	0.94	0.96	+2%	0.92	0.94	+2%
Elongation	0.29	0,3	+3%	0.29	0.28	−3%
VA3d	13	18.5	**+42%**	4.7	9.5	**+102%**
θ (°)	0	0	-	0	0	-
φ (°)	67	60	**−10%**	73	69	**−5%**

Note. Parameters that show significant variation are in bold characters. Monz.3: sample Monzonite 3. Monz. 4: sample Monzonite 4, σ_f: differential stress at failure. See text for the definitions of the parameters.

opened perpendicular to σ_3 with increasing stress toward failure. This interpretation is confirmed by the variation of the shape parameter VA3d, which increases towards failure (Figure 7b). Although both the porosity and the volumetric strain evolutions show dilatancy (Figures 2d and 4a), this dilatant behavior occurs mainly by increasing the size of preexisting microfractures augmented by a moderate increase of the aperture of the microfractures. A possible interpretation is also that stress screening occurs, which prevents the opening of existing microfractures.

The evolution of the mean orientation of the microfractures shows two features. The angle φ is more or less constant below the yield point and shows an average value around 70°. This indicates the existence of both microfractures parallel to σ_1, with $\varphi = 90°$, and other microfractures in various orientations. This is confirmed by the probability density function of φ (Figures 8e and 8f), which shows a maximum at 90° and a decreasing number of microfractures with lower angles. The peak at 90° decreases significantly when approaching failure. This can be interpreted by the linkage of mostly vertical parallel wing cracks along a fault (Ashby & Sammis, 1990), resulting in single microfracture with an average orientation smaller than 90°. The evolution of the angle θ shows on average a constant value close to 0. This indicates that the vertical microfractures are oriented with a similar probability in all directions in a plane perpendicular to σ_1, as observed on Figure 4b. However, the probability density function of θ includes more details with the emergence of two peaks (black arrows in Figures 8g and 8h), which we interpret to correspond to the development of vertical microfractures in directions that correspond to the future shear fault planes.

4. Discussion

4.1. Models of Failure of Rocks

Failure of materials has been described by several mechanical models since the fifteenth century (see review by Alava et al., 2006), and the main concepts and predictions of recent models are summarized in Figure 9. The new information obtained with X-ray microtomography discussed here is the statistical distributions and geometrical properties of voids or microfractures. Consider the size $S(\sigma)$ of a microfracture observed on a scan at a differential stress σ in voxels (i.e., a volume). This microfracture may have grown from the beginning of the test by increments $\Delta S(\sigma)$ observed between tomography scan at $\sigma - d\sigma$ and scan at σ. In the X-ray tomography data, S can be extracted at each stress step directly, but not ΔS, owing to the global deformation of the sample. From the knowledge of S values, three parameters are calculated or deduced: the damage index D_ϕ, its incremental rate with respect to differential stress $\frac{dD_\phi}{d\Delta}$, and the size of the largest microfracture S_ϕ. When discussing a subcritical crack growth mechanism, or an analogy with percolation, S is an appropriate variable. This is less obvious when considering a critical phase transition, or an analogy with earthquake dynamics, where ΔS is more appropriate because this quantity represents increments of strain. Such increments of strains are recorded in earthquake catalogues where each earthquake represents an incremental growth of a fault.

The X-ray tomography data allow tracking the evolution of D_ϕ, its associated rate, and S_ϕ with increasing stress (Figures 5 and 6), and our results point to a power law divergence of these variables toward failure.

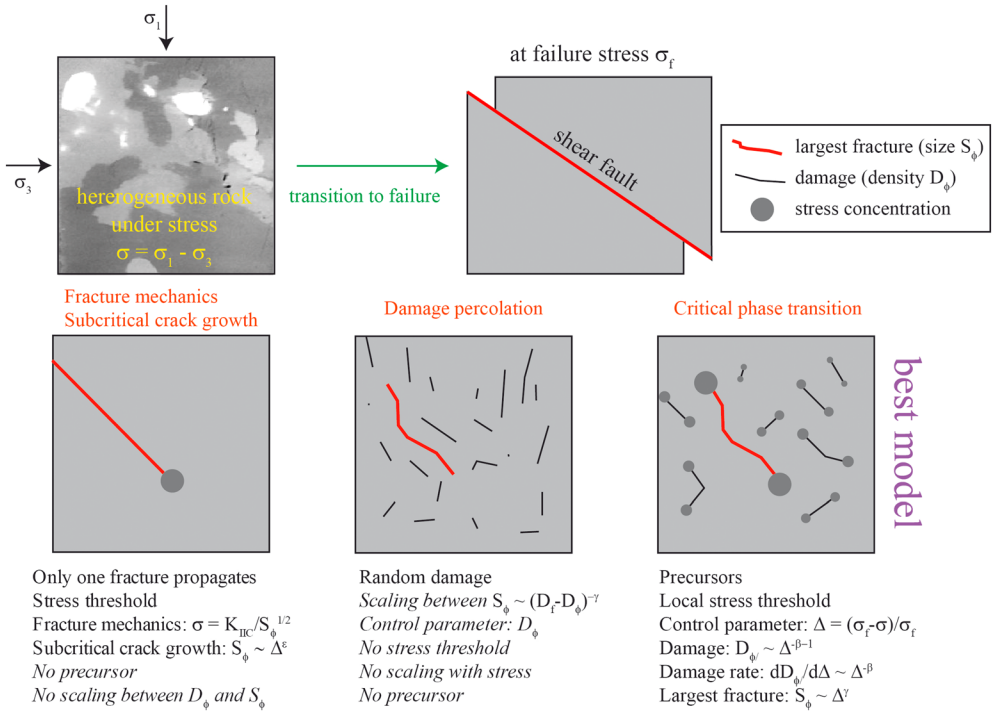

Figure 9. Models of failure in heterogeneous rocks. (top) The rock under stress evolves toward a faulted state. (bottom) Three categories of models used to explain fracturing and faulting and corresponding scaling relationships. The predictions of these models are indicated (in italic predictions that are contradicted by the present study).

This can then be compared with predictions from the following theories proposed to explain the failure of materials: (i) classical fracture mechanics, (ii) subcritical crack growth, (iii) percolation theory, and (iv) dynamical critical phase transition. For some of these theories, one expects $\frac{dD_\phi}{d\Delta}$ and S_ϕ to diverge when approaching failure (i.e., when $\Delta \rightarrow 0$). In what follows, we do not consider the dependence of distributions or parameters upon the global system size, as the rock sample size was not varied in the experiments. From the X-ray data, this does not seem to be a crucial issue because the sample size is much larger than the largest microfracture.

4.1.1. Fracture Mechanics Model

In this approach the fault is assumed to propagate as a mode II shear crack, as soon as the stress intensity factor at the tip of an existing defect of length l_0 reaches the shear toughness of the material, K_{IIc}. Note that if one assumes an ellipsoidal void in an elastic medium, then $S \sim l^3$ where l is the major axis of the ellipse representing the fault "length." In this case, if one neglects disorder of toughness (i.e., K_{IIc} is constant), one should expect (i) only one crack in the sample; (ii) nothing happens as long as $K_{II} < K_{IIc}$, that is, $\sigma < A\frac{K_{IIc}}{l^{1/2}}$, where A is a geometrical constant; and (iii) the fault should propagate suddenly in an inertial regime when $\sigma = A\frac{K_{IIc}}{l^{1/2}}$, without any precursory signal. In other words, failure appears a first-order transition in this case. This approach cannot explain the observations of the present experiments such as multiple cracks, clusters, and precursors, so it can be eliminated.

4.1.2. Subcritical Crack Growth Model

In this approach, one considers a single-mode II shear defect of initial length l_0, which propagates in a subcritical, quasi-static regime ($K_{II} < K_{IIc}$). In this case $\frac{dl}{dt} = BK_{II}^n$, where B is a constant and n an exponent generally very large, between 10 and 50 (e.g., (Atkinson, 1979)). The supporting information provides a derivation for the relation between the largest cluster (the unique crack) and stress, following previous derivation for a constant stress (creep) (Weiss, 2004). The final result is $S_\varphi \sim \Delta^{-\left(\frac{6}{n-2}\right)}$, which might appear compatible with our observations (see section 3.2 and Figure 5b). However, in this case, the damage reduces to a single crack, that is, $D_\phi = S_\phi$. Such approach is incompatible, by construction, with a power law distribution of cluster sizes (Figures 8a and 8b) as there is only one cluster. The subcritical crack model assumes a very strong

anisotropy of damage, concentrated along an almost 2D crack. It reproduces a power law divergence of the largest microfracture at failure, but neither the numerous precursors observed in the experiments, nor the observed nontrivial scaling $S_\phi \sim D_\phi^{\alpha}$ with $\alpha < 1$.

4.1.3. Percolation Theory Model

In contrast to the previous models, which ignore the presence of microstructural disorder (except for the presence of an initial defect l_0), the problem of the failure of heterogeneous media can be mapped onto the percolation problem in case of infinite disorder (Roux et al., 1988). Here bonds break randomly; that is, there is no mechanical interaction between microfractures. Disorder is understood as an initial distribution of local strengths. For infinite disorder, as the stress is increased, bonds fail one after another, simply following the hierarchy dictated by the distribution of local strengths (the weakest bond first), without any influence of stress redistributions.

Unlike the fracture mechanics model mentioned above, percolation can describe a critical transition, with power law divergence of the largest cluster when approaching the percolation threshold. However, if S_φ can be considered as the order parameter of this critical transition, the control parameter is not the stress, but the probability p for a site to be "broken," that is, our damage index D_ϕ. Classical percolation theory predicts (e.g., Aharony & Stauffer, 2003; Stauffer, 1979) $S_\varphi \sim (p_c - p)^{-\gamma} \sim (D_f - D_\phi)^{-\gamma}$, with D_f as the damage index at the percolation threshold (failure) and $\gamma \approx 2.2$ in three dimensions. This scaling is in fundamental disagreement with our observations, $S_\phi \sim D_\phi^{\alpha}$. In addition, percolation theory cannot explain a power law divergence of the damage rate or of the global damage D_ϕ, as the "damage" itself is the control parameter.

4.1.4. Critical Phase Transition Model

The observed damage patterns (section 3.1) as well as the discussion above demonstrate that the faulting process can neither correspond to a single crack growth nor be mapped to a simple percolation problem. In other words, both disorder and mechanical interactions are important in the route toward failure. This is reminiscent of a dynamical phase transition in which three fundamental concepts are involved: (i) a local threshold mechanics as local microcracking occurs when a local strength threshold is reached, (ii) the existence of disorder associated with a distribution of local strengths, and (iii) elastic long-ranged interactions (i.e., elastic interactions that decrease as $1/r^b$ where r is the distance away from a defect and b is an exponent equal to or greater than 1 that depends on the dimensionality of the system and of the defect). These ingredients are generic for many problems, including the propagation of a crack front within a heterogeneous material characterized by disorder on local toughness (Bonamy & Bouchaud, 2011). This last point is an important difference with the frameworks of fracture mechanics and subcritical crack growth.

One paradigm for such a process is the so-called depinning transition (Fisher, 1998). The problem of fault slip was mapped onto this depinning transition by Fisher et al. (1997), while Weiss et al. (2014) proposed a similar mapping for the compression failure of brittle heterogeneous materials (including rocks), that is, the process analyzed here. The depinning problem is a dynamical transition separating an "arrested" (unfailed) state from a dynamical (failed) state throughout a threshold (the failure stress in our case) partly depending on the initial disorder. It gives predictions for the evolution toward the critical point of the distribution of avalanche sizes or energies. This is related in our case to individual microcrack growth increments, that is, ΔS with our notation, while the present tomographic data refer to the cumulative evolution of the microcracks from the onset of loading, S.

Hence, a direct comparison between the depinning scenario and our problem is not straightforward, calling for further data acquisition and processing development of the X-ray microtomography data where individual microfractures would be followed and the increments of growth would be measured at higher precision. However, the evolution of avalanche distributions translated in terms of a power law divergence of the damage $\frac{dD_\phi}{d\Delta}$ and the energy release $\frac{dE}{d\Delta}$ rates (Girard et al., 2010) is fully compatible with our results (see section 3.2).

A mean-field description of depinning has been proposed by LeBlanc et al. (2013), with associated exponent values translating into a damage rate divergence $\frac{dD_\phi}{d\Delta} \sim -\Delta^{-1}$, that is, an exponent $\beta = 1$ smaller than our reported values. Although a complete mapping of our problem onto the depinning transition is not possible, owing to the nature of our (cumulative) data, the analogy described above strongly suggests an interpretation of the faulting process as a critical transition.

4.2. Damage Models and Criticality

In the present experiments, several microfractures form at a given stress step, and there is a progressive growth and linkage of them as observed previously (Lockner et al., 1991; Reches & Lockner, 1994). Damage starts developing below the Coulomb threshold (Figures 1c and S1c) indicating the importance of distributed microcracks that evolve and lead to the final macroscopic rupture. Failure occurs by progressive development of damage and localization along a future shear fault. Damage rheology models account for progressive evolution of distributed cracking that couple internal stress redistribution and changes of elastic moduli until localization (e.g., Amitrano et al., 1999; Girard et al., 2010; Lyakhovsky et al., 1997, 2011). In these models, failure is the consequence of the nucleation, growth, interaction, and coalescence of rock damage. Several models reproduce power law increase of damage towards failure (Amitrano et al., 1999; Ben-Zion & Lyakhovsky, 2002; Girard et al., 2012; Kun et al., 2014; Turcotte et al., 2003). In statistical physics, such a power law divergence is characteristic of second-order (critical) phase transition. These systems show emergent behavior with power law evolution of internal parameters with respect to a control parameter that corresponds to the distance from the critical point. In the present case, the control parameter is Δ, and two-order parameters, the damage index and the size of the largest microfracture, show power law divergence when approaching failure. Various models of critical phenomenon have been proposed to explain the dynamics of earthquakes (Ben-Zion et al., 2003; Dahmen et al., 2009; Fisher et al., 1997; Main, 1995; Rundle et al., 2003; Sornette & Sammis, 1995). The data of the present study are discussed with respect to critical damage evolution.

The total volume of porosity, measured as a damage index (Figures 5a and 5b), the damage growth rate, and the size of the largest fracture (Figure 5c) all diverge toward failure, following a power law evolution. These results are consistent with the damage model of Girard et al. (2010, 2012). The average values of the three eigenvalues of the microfracture covariance matrix, the flatness, and the shape factor show also increasing acceleration toward failure (Table 2 and Figure 7). The orientations of the microfractures evolve with the average φ angle that decreases due to fracture linkage and θ angle that shows the emergence of the largest microfracture that becomes later the main shear fault (Figure 8). The largest cluster in the damage model of Girard et al. (2012) grows as a power law, with an exponent γ between 1.3 and 1.6, depending on the amount of disorder in the system. This divergence results from both the coalescence and the growth of existing microfractures. In the present experiments, this process of microfracture growth can be directly observed and quantified. The size of the largest cluster diverges toward failure, in agreement with progressive damage models (Girard et al., 2012) though with smaller γ values, between 0.3 and 0.4 (Figure 5c).

In laboratory failure experiments of heterogeneous materials such as wood, plaster, or fiberglass samples loaded in mode I, the cumulated released acoustic energy E shows a power law increase toward failure $E \sim \Delta^{-\beta+1}$ with an exponent $\beta - 1$ in the range 0.22–0.27, corresponding to a critical exponent β for the energy release rate around 1.25 (Garcimartin et al., 1997). Our results for D_ϕ are compatible with this framework, although the present experiments were performed under compressional loading conditions, whereas Garcimartin et al. (1997) performed experiments under tensile loading conditions. All of this argues for the interpretation of the compressive failure of quartz-monzonite as a critical transition.

4.3. Implications for Earthquake Mechanics

In the context of earthquakes, power law increase of seismicity parameters and functions before major ruptures have been reported in various studies (e.g., Keilis-Borok & Kossobokov, 1990; Rundle et al., 2003; Zöller & Hainzl, 2002). However, such behavior is not always observed because of a combination of limited resolution of the recorded seismic data coupled with the diversity of earthquake processes (e.g., Ben-Zion, 2008). The most commonly observed precursory behavior is associated with foreshocks that sometimes follow an inverse Omori-type law $\Delta N/\Delta t = K(c + t_M - t)^{-q}$, where $q \approx 1$ (e.g., Jones & Molnar, 1979; Papazachos, 1973). However, systematic analyses of seismicity clusters at regional and global scales demonstrate that the phenomenology of foreshocks is not universal (Zaliapin & Ben-Zion, 2013a, 2013b, 2016). Another precursory seismic activity that has been reported in numerous studies involves a power law time-to-failure relation of the cumulative Benioff strain $\sum_{t_i<t} M_0^{1/2}(t_i) = A + B(t_f - t)^m$, where M_0 is the seismic moment and $m \approx 1/3$ (e.g., Bufe & Varnes, 1993; Jaumé & Sykes, 1999). Fits of data indicate that B is typically negative, showing

an increase of Benioff strain toward failure. However, subsequent studies showed that these reports can result from improper accounting for expectations associated with random fluctuations (Hardebeck et al., 2008).

The direct comparison of the experimental data of the present study with seismic catalogues is challenging for two main reasons: (1) the experimental data represent the cumulative growth of damage without separating growth increments for individual microfractures and (2) the experimental data include both seismic and aseismic strain, whereas seismic catalogues record only the seismic component of deformation. The results of Figure 5b show that the cumulative volume of damage in the quartz-monzonite evolves with a power law with exponent $\beta - 1$ in the range 0.4 to 0.8. Here the distance to failure is not time, as for earthquake catalogues, but the distance from the stress at failure. Since the quantities analyzed in Figure 5 (damage index and maximum cluster size) and control parameter (distance to failure) are different from those used in analysis and models of seismicity, it is difficult to make direct comparisons. Nevertheless, the progressive failure and localization process in the experiments analyzed in the present study are similar to reported forms of accelerated seismic activity before large earthquakes in some models of earthquakes, other experimental results, and seismic data. This provides renewed impetus for continuing analyses of laboratory experiments, models, and seismic data to clarify further the evolution leading to large failure events.

The direct imaging of the evolving microcracks presented here indicates that compressive shear failure is associated with a complex cumulative process involving nucleation processes, long-range interactions, and coalescence of microfractures, leading to system-size faulting of the sample. The observed average decrease of flatness of the microfractures before the macroscopic failure (Figure 7a) is consistent with increasing dilation reported in various previous fracturing experiments (e.g., Brace et al., 1966; Stanchits et al., 2006) and measured on the two samples (Figure 2d). The data of the present paper show that such dilation occurs more by increasing the surface of the microfractures along the first two eigenvalues rather than by increasing their aperture (i.e., third eigenvalue). These observations motivate also analysis of evolving earthquake focal mechanisms with particular attention to isotropic source terms (e.g., Ben-Zion & Ampuero, 2009; Martínez-Garzón et al., 2017; Ross et al., 2015) and monitoring temporal changes of seismic velocities including anisotropy (Obermann et al., 2014; Saade et al., 2017). Such studies are even more challenging than analyses of seismicity parameters, but improved data sets and techniques offer currently better possibilities for observing these properties than existed before.

5. Conclusions

The evolution of damage prior to failure was imaged in two quartz-monzonite samples with high time and spatial resolution and under in situ stress conditions. By using time-lapse three-dimensional X-ray microtomography imaging, with a voxel resolution of 6.5 μm, the microfractures were extracted at each stress step. The evolutions of several geometrical parameters between yielding and faulting stresses were characterized, and their dynamics allow quantifying how precursors self-organize before faulting. The main results are the following:

- The damage index, its growth rate, and the size of the largest microfracture show a power law divergence toward faulting, in agreement with statistical physics models that consider rupture as a critical phenomenon. The data provide the first experimental confirmation of such models where the power law divergence of both the damage rate and the size of the largest microfracture toward failure are reported together.
- The distribution and mean of several geometrical parameters of the damage prior to failure were quantified. Among these quantities the flatness of the microfractures shows a significant decrease when approaching failure. This indicates that dilatancy is dominated by the growth of planar microfractures in their main plane rather than by increasing their aperture.
- The average orientation of the microfractures shows an evolution when approaching faulting and is interpreted as the linkage of mode I microfractures.

The high spatial resolution of X-ray microtomography data allows to quantify damage prior to failure with unprecedented details. Further developments of this experimental technique will involve adding acoustic emission recording, refining the time scale between each three-dimensional acquisitions to better characterize the development of damage very close to failure, and data mining such that each single microfracture and

its increment of growth could be followed in time. This will allow more direct comparisons with analyses of earthquake catalogues. The presented results call for joint analyses of seismicity parameters, volumetric deformation (not only shear), temporal changes of seismic velocities, and anisotropy development before large earthquakes.

Acknowledgments

The deformation apparatus was built by Sanchez Technology. Elodie Boller, Paul Tafforeau, and Alexander Rack provided advice on the design of the tomography setup. This study received funding from the Norwegian Research Council (project HADES, grant 250661) and the European Union's Horizon 2020 Research and Innovation Programme under the ERC Advanced Grant Agreement 669972, "Disequilibrium Metamorphism' ("DIME"). Beamtime was allocated at the European Synchrotron Radiation Facility (Long Term Proposal ES-295). Data storage was provided by UNINETT Sigma2—the National Infrastructure for High Performance Computing and Data Storage in Norway (project NS9073K). The X-ray tomography data (series of 3D volumes, 16 bytes gray scale) supporting the conclusions can be downloaded from Renard et al., (2017). Critical evolution of damage toward system-size failure in a crystalline rock (Data set). Norstore. https://doi.org/10.11582/2017.00025.

References

Aben, F. M., Doan, M.-L., Mitchell, T. M., Toussaint, R., Reuschlé, T., Fondriest, M., et al. (2016). Dynamic fracturing by successive coseismic loadings leads to pulverization in active fault zones. *Journal of Geophysical Research: Solid Earth*, *121*, 2338–2360. https://doi.org/10.1002/2015JB012542

Aharony, A., & Stauffer, D. (2003). *Introduction to Percolation Theory*. London: Taylor & Francis.

Alava, M. J., Nukala, P. K. V. V., & Zapperi, S. (2006). Statistical model of fractures. *Advances in Physics*, *55*(3-4), 349–476. https://doi.org/10.1080/00018730300741518

Amitrano, D., Grasso, J. R., & Hantz, D. (1999). From diffuse to localized damage through elastic interaction. *Geophysical Research Letters*, *26*(14), 2109–2112. https://doi.org/10.1029/1999GL900388

Amitrano, D., Grasso, J. R., & Senfaute, G. (2005). Seismic precursory patterns before a cliff collapse and critical point phenomena. *Geophysical Research Letters*, *32*, L08314. https://doi.org/10.1029/2004GL022270

Ashby, M. F., & Sammis, C. G. (1990). The damage mechanics of brittle solids in compression. *Pure and Applied Geophysics*, *133*(3), 489–521. https://doi.org/10.1007/BF00878002

Atkinson, B. K. (1979). A fracture mechanics study of subcritical tensile cracking of quartz in wet environments. *Pure and Applied Geophysics*, *117*(5), 1011–1024. https://doi.org/10.1007/BF00876082

Benson, P. M., Vinciguerra, S., Meredith, P. G., & Young, R. P. (2008). Laboratory simulation of volcano seismicity. *Science*, *322*(5899), 249–252. https://doi.org/10.1126/science.1161927

Ben-Zion, Y. (2008). Collective behavior of earthquakes and faults: Continuum-discrete transitions, progressive evolutionary changes, and different dynamic regimes. *Reviews of Geophysics*, *46*, RG4006. https://doi.org/10.1029/2008RG000260

Ben-Zion, Y., & Ampuero, J.-P. (2009). Seismic radiation from regions sustaining material damage. *Geophysical Journal International*, *178*(3), 1351–1356. https://doi.org/10.1111/j.1365-246X.2009.04285.x

Ben-Zion, Y., & Lyakhovsky, V. (2002). Accelerated seismic release and related aspects of seismicity patterns on earthquake faults. *Pure and Applied Geophysics*, *159*, 2385–2412.

Ben-Zion, Y., Eneva, M., & Liu, Y. (2003). Large earthquake cycles and intermittent criticality on heterogeneous faults due to evolving stress and seismicity. *Journal of Geophysical Research*, *108*(B6), 2307. https://doi.org/10.1029/2002JB002121

Bonamy, D., & Bouchaud, B. (2011). Failure of heterogeneous materials: A dynamic phase transition? *Physics Reports*, *498*(1), 1–44. https://doi.org/10.1016/j.physrep.2010.07.006

Bouchon, M., Karabulut, H., Aktar, M., Özalaybey, S., Schmittbuhl, J., & Bouin, M. P. (2011). Extended nucleation of the 1999 Mw 7.6 Izmit earthquake. *Science*, *331*(6019), 877–880. https://doi.org/10.1126/science.1197341

Bouchon, M., Durand, V., Marsan, D., Karabulut, H., & Schmittbuhl, J. (2013). The long precursory phase of most large interplate earthquakes. *Nature Geoscience*, *6*(4), 299–302. https://doi.org/10.1038/ngeo1770

Brace, W. F., Paulding, B. W. Jr., & Scholz, C. H. (1966). Dilatancy in the fracture of crystalline rocks. *Journal of Geophysical Research*, *71*(16), 3939–3953. https://doi.org/10.1029/JZ071i016p03939

Buades, A., Coll, B., & Morel, J. M. (2005). A non-local algorithm for image denoising, In Computer Vision and Pattern Recognition. *IEEE Computer Society Conference*, *2*, 60–65.

Bufe, C. G., & Varnes, D. J. (1993). Predictive modeling of the seismic cycle of the great San Francisco bay region. *Journal of Geophysical Research*, *98*(B6), 9871–9883. https://doi.org/10.1029/93JB00357

Candela, T., & Renard, F. (2012). Segment linkage process at the origin of slip surface roughness: Evidence from the Dixie Valley fault. *Journal of Structural Geology*, *45*, 87–100. https://doi.org/10.1016/j.jsg.2012.06.003

Christensen, K., & Moloney, N. R. (2005). *Complexity and Criticality* (Vol. 1). London: Imperial college press.

Cowie, P. A., & Scholz, C. H. (1992). Growth of faults by accumulation of seismic slip. *Journal of Geophysical Research*, *97*, 11,085–11,095.

Dahmen, K. A., Ben-Zion, Y., & Uhl, J. T. (2009). A micromechanical model for deformation in disordered solids with universal predictions for stress-strain curves and related avalanches. *Physical Review Letters*, *102*(17), 2009. https://doi.org/10.1103/PhysRevLett.102.175501

de Arcangelis, J., Godano, C., Grasso, J. R., & Lippiello, E. (2016). Statistical physics approach to earthquake occurrence and forecasting. *Physics Reports*, *628*, 1–91. https://doi.org/10.1016/j.physrep.2016.03.002

Desrues, J., Chambon, R., Mokni, M., & Mazerolle, F. (1996). Void ratio evolution inside shear bands in triaxial sand specimens studied by computed tomography. *Geotechnique*, *46*(3), 529–546. https://doi.org/10.1680/geot.1996.46.3.529

Du, Y., & Aydin, A. (1991). Interaction of multiple cracks and formation of echelon crack arrays. *International Journal of Numerical and Analytical Methods in Geomechanics*, *15*, 205e218.

Fisher, D. S. (1998). Collective transport in random media: From superconductors to earthquakes. *Physics Reports*, *301*(1-3), 113–150. https://doi.org/10.1016/S0370-1573(98)00008-8

Fisher, D. S., Dahmen, K., Ramanathan, S., & Ben-Zion, Y. (1997). Statistics of earthquakes in simple models of heterogeneous faults. *Physical Review Letters*, *78*(25), 4885–4888. https://doi.org/10.1103/PhysRevLett.78.4885

Garcimartin, A., Guarino, A., Bellon, L., & Cilberto, S. (1997). Statistical properties of fracture precursors. *Physical Review Letters*, *79*(17), 3202–3205. https://doi.org/10.1103/PhysRevLett.79.3202

Girard, L., Amitrano, D., & Weiss, J. (2010). Failure as a critical phenomenon in a progressive damage model. *Journal of Statistical Mechanics: Theory and Experiment*, *P01013*.

Girard, L., Weiss, J., & Amitrano, D. (2012). Damage-cluster distributions and size effect on strength in compressive failure. *Physical Review Letters*, *108*(22), 225,502. https://doi.org/10.1103/PhysRevLett.108.225502

Goebel, T. H. W., Becker, T. W., Schorlemmer, D., Stanchits, S., Sammis, C., Rybacki, E., & Dresen, G. (2012). Identifying fault heterogeneity through mapping spatial anomalies in acoustic emission statistics. *Journal of Geophysical Research*, *117*, B03310. https://doi.org/10.1029/2011JB008763

Hamiel, Y., Lyakhovsky, V., Stanchits, S., Dresen, G., & Ben-Zion, Y. (2009). Brittle deformation and damage-induced seismic wave anisotropy in rocks. *Geophysical Journal International*, *178*(2), 901–909. https://doi.org/10.1111/j.1365-246X.2009.04200.x

Hardebeck, J. L., Felzer, K. R., & Michael, A. J. (2008). Improved tests reveal that the accelerating moment release hypothesis is statistically insignificant. *Journal of Geophysical Research*, *113*, B08310. https://doi.org/10.1029/2007JB005410

Herrmann, H. J., & Roux, S. (1990). *Statistical Models for the Fracture of Disordered Media*. Amsterdam: North-Holland.

Jaumé, S. C., & Sykes, L. R. (1999). Evolving towards a critical point: A review of accelerating seismic moment/energy release prior to large and great earthquakes. In *Seismicity Patterns, their Statistical Significance and Physical Meaning* (pp. 279–305). Basel: Birkhaüser.

Jones, L. M., & Molnar, P. (1979). Some characteristics of foreshocks and their possible relationship to earthquake prediction and premonitory slip on faults. *Journal of Geophysical Research*, *84*, 3596–3608.

Kato, A., Fukuda, J. I., Nakagawa, S., & Obara, K. (2016). Foreshock migration preceding the 2016 Mw 7.0 Kumamoto earthquake, Japan. *Geophysical Research Letters*, *43*, 8945–8953. https://doi.org/10.1002/2016GL070079

Keilis-Borok, V. I., & Kossobokov, V. G. (1990). Premonitory activation of earthquake flow: Algorithm M8. *Physics of the Earth and Planetary Interiors*, *61*(1-2), 73–83. https://doi.org/10.1016/0031-9201(90)90096-G

Kun, F., Varga, I., Lennartz-Sassinek, S., & Main, I. G. (2014). Rupture cascades in a discrete element model of a porous sedimentary rock. *Physical Review Letters*, *112*(6), 065501. https://doi.org/10.1103/PhysRevLett.112.065501

LeBlanc, M., Angheluta, L., Dahmen, K., & Goldenfeld, N. (2013). Universal fluctuations and extreme statistics of avalanches near the depinning transition. *Physical Review E*, *87*(2), 022126. https://doi.org/10.1103/PhysRevE.87.022126

Lindanger, M., Gabrielsen, R. H., & Braathen, A. (2007). Analysis of rock lenses in extensional faults. *Norwegian Journal of Geology*, *87*, 361–372.

Lockner, D., Byerlee, J. D., Kuksenko, V., Ponomarev, A., & Sidorin, A. (1991). Quasi-static fault growth and shear fracture energy in granite. *Nature*, *350*(6313), 39–42. https://doi.org/10.1038/350039a0

Lyakhovsky, V., Ben-Zion, Y., & Agnon, A. (1997). Distributed damage, faulting, and friction. *Journal of Geophysical Research*, *102*, 27,635–27,649.

Lyakhovsky, V., Hamiel, Y., & Ben-Zion, Y. (2011). A non-local visco-elastic damage model and dynamic fracturing. *Journal of the Mechanics and Physics of Solids*, *59*(9), 1752–1776. https://doi.org/10.1016/j.jmps.2011.05.016

Main, I. G. (1995). Earthquakes as critical phenomena: Implications for probabilistic seismic hazard analysis. *Bulletin of the Seismological Society of America*, *85*, 1299–1308.

Martínez-Garzón, P., Kwiatek, G., Bohnhoff, M., & Dresen, G. (2017). Volumetric components in the earthquake source related to fluid injection and stress state. *Geophysical Research Letters*, *44*, 800–809. https://doi.org/10.1002/2016GL071963

Mirone, A., Brun, E., Gouillart, E., Tafforeau, P., & Kieffer, J. (2014). The PyHST2 hybrid distributed code for high speed tomographic reconstruction with iterative reconstruction and a priori knowledge capabilities. *Nuclear Instruments and Methods in Physics Research Section B: Beam Interactions with Materials and Atoms*, *324*, 41–48. https://doi.org/10.1016/j.nimb.2013.09.030

Obermann, A., Froment, B., Campillo, M., Larose, E., Planès, T., Valette, B., et al. (2014). Seismic noise correlations to image structural and mechanical changes associated with the Mw7.9 2008 Wenchuan earthquake. *Journal of Geophysical Research: Solid Earth*, *119*, 3155–3168. https://doi.org/10.1002/2013JB010932

Otsuki, K., & Dilov, T. (2005). Evolution of hierarchical self-similar geometry of experimental fault zones: Implications for seismic nucleation and earthquake size. *Journal of Geophysical Research*, *110*, B03303. https://doi.org/10.1029/2004JB003359

Papazachos, B. C. (1973). The time distribution of reservoir-associated foreshocks and its importance to the prediction of the principal shock. *Bulletin of the Seismological Society of America*, *63*, 1973–1978.

Paterson, M. S., & Wong, T. F. (2005). *Experimental Rock Deformation-the Brittle Field*. New York: Springer.

Reches, Z., & Lockner, D. A. (1994). Nucleation and growth of faults in brittle rocks. *Journal of Geophysical Research*, *99*(B9), 18159–18173. https://doi.org/10.1029/94JB00115

Renard, F., Bernard, D., Thibault, X., & Boller, E. (2004). Synchrotron 3D microtomography of halite aggregates during experimental pressure solution creep and evolution of the permeability. *Geophysical Research Letters*, *31*, L07607. https://doi.org/10.1029/2004GL019605

Renard, F., Bernard, D., Desrues, J., & Ougier-Simonin, A. (2009). 3D imaging of fracture propagation using synchrotron X-ray microtomography. *Earth and Planetary Science Letters*, *286*(1-2), 285–291. https://doi.org/10.1016/j.epsl.2009.06.040

Renard, F., Cordonnier, B., Dysthe, D. K., Boller, E., Tafforeau, P., & Rack, A. (2016). A deformation rig for synchrotron microtomography studies of geomaterials under conditions down to 10 km depth in the Earth. *Journal of Synchrotron Radiation*, *23*(4), 1030–1034. https://doi.org/10.1107/S1600577516008730

Renard, F., Cordonnier, B., Kobchenko, M., Kandula, N., Weiss, J., & Zhu, W. (2017). Microscale characterization of rupture nucleation unravels precursors to faulting in rocks. *Earth and Planetary Science Letters*, *476*, 69–78. https://doi.org/10.1016/j.epsl.2017.08.002

Ross, Z. E., Ben-Zion, Y., & Zhu, L. (2015). Isotropic source terms of San Jacinto fault zone earthquakes based on waveform inversions with a generalized CAP method. *Geophysical Journal International*, *200*(2), 1269–1280. https://doi.org/10.1093/gji/ggu%20460

Roux, S., Hansen, A., Herrmann, H., & Guyon, E. (1988). Rupture of heterogeneous media in the limit of infinite disorder. *Journal of Statistical Physics*, *52*(1-2), 237–244. https://doi.org/10.1007/BF01016411

Rundle, J. B., Turcotte, D. L., Shcherbakov, R., Klein, W., & Sammis, C. (2003). Statistical physics approach to understanding the multiscale dynamics of earthquake fault systems. *Reviews of Geophysics*, *41*(4), 1019. https://doi.org/10.1029/2003RG000135

Saade, M., Montagner, J. P., Roux, P., Shiomi, K., Enescu, B., & Brenguier, F. (2017). Monitoring of seismic anisotropy at the time of the 2008 Iwate-Miyagi (Japan) earthquake. *Geophysical Journal International*, *211*(1), 483–497. https://doi.org/10.1093/gji/ggx321

Sammis, C. G., & Smith, S. W. (1999). Seismic cycles and the evolution of stress correlation in cellular automaton models of finite fault networks. *Pure and Applied Geophysics*, *155*, 307–334.

Schubnel, A., & Guéguen, Y. (2013). Dispersion and anisotropy of elastic waves in cracked rocks. *Journal of Geophysical Research: Solid Earth*, *108*, 2101. https://doi.org/10.1029/2002JB001824

Schubnel, A., Thompson, B. D., Fortin, J., Guéguen, Y., & Young, R. P. (2007). Fluid-induced rupture experiment on Fontainebleau sandstone: Premonitory activity, rupture propagation, and aftershocks. *Geophysical Research Letters*, *34*, L19307. https://doi.org/10.1029/2007GL031076

Sornette, D., & Sammis, C. (1995). Complex critical exponents from renormalization group theory of earthquakes: Implications for earthquake predictions. *Journal de Physique*, *5*, 607–619.

Stanchits, S., Vinciguerra, S., & Dresen, G. (2006). Ultrasonic velocities, acoustic emission characteristics and crack damage of basalt and granite. *Pure and Applied Geophysics*, *163*(5-6), 975–994. https://doi.org/10.1007/s00024-006-0059-5

Stauffer, D. (1979). Scaling theory of percolation clusters. *Physics Reports*, *54*(1), 1–74. https://doi.org/10.1016/0370-1573(79)90060-7

Sugan, M., Kato, A., Miyake, H., Nakagawa, S., & Vuan, A. (2014). The preparatory phase of the 2009 Mw 6.3 L'Aquila earthquake by improving the detection capability of low-magnitude foreshocks. *Geophysical Research Letters*, *41*, 6137–6144. https://doi.org/10.1002/2014GL061199

Turcotte, D. L., Newman, W. I., & Shcherbakov, R. (2003). Micro and macroscopic models of rock fracture. *Geophysical Journal International*, *152*(3), 718–728. https://doi.org/10.1046/j.1365-246X.2003.01884.x

Weiss, J. (2004). Subcritical crack propagation as a mechanism of crevasse formation and iceberg calving. *Journal of Glaciology*, *50*(168), 109–115. https://doi.org/10.3189/172756504781830240

Weiss, J., Girard, L., Gimbert, F., Amitrano, D., & Vandembroucq, D. (2014). (Finite) statistical size effects on compressive strength. *Proceedings of the National Academy of Sciences*, *111*(17), 6231–6236. https://doi.org/10.1073/pnas.1403500111

Wu, C., Peng, Z., Meng, X., & Ben-Zion, Y. (2014). Lack of spatio-temporal localization of foreshocks before the 1999 Mw7.1 Duzce, Turkey earthquake. *Bulletin of the Seismological Society of America*, *104*(1), 560–566. https://doi.org/10.1785/0120130140

Zaliapin, I., & Ben-Zion, Y. (2013a). Earthquake clusters in southern California I: Identification and stability. *Journal of Geophysical Research: Solid Earth*, *118*, 2847–2864. https://doi.org/10.1002/jgrb.50179

Zaliapin, I., & Ben-Zion, Y. (2013b). Earthquake clusters in southern California II: Classification and relation to physical properties of the crust. *Journal of Geophysical Research: Solid Earth*, *118*, 2865–2877. https://doi.org/10.1002/jgrb.50178

Zaliapin, I., & Ben-Zion, Y. (2016). A global classification and characterization of earthquake clusters. *Geophysical Journal International*, *207*(1), 608–634. https://doi.org/10.1093/gji/ggw300

Zang, A., Wagner, F. C., Stanchits, S., Janssen, C., & Dresen, G. (2000). Fracture process zone in granite. *Journal of Geophysical Research*, *105*, 23,651–23,661.

Zhu, W., Fusseis, F., Lisabeth, H., Xing, T., Xiao, X., De Andrade, V., & Karato, S. (2016). Experimental evidence of reaction-induced fracturing during olivine carbonation. *Geophysical Research Letters*, *18*, 9535–9543. https://doi.org/10.1002/2016GL070834

Zöller, G., & Hainzl, S. (2002). A systematic spatiotemporal test of the critical point hypothesis for large earthquakes. *Geophysical Research Letters*, *29*(11), 1558. https://doi.org/10.1029/2002GL014856